Supplementary Information (SI) for EES Batteries.
This journal is © The Royal Society of Chemistry 2026

†Electronic Supplementary Information

Anomalous Pseudocapacitance of Vanadium Carbide MXene in Water-in-Salt Electrolytes

Rituprava Dash[‡a], *Suman Yadav*[‡a], *and Narendra Kurra**[a]

---

[a] *Department of Chemistry, Indian Institute of Technology Hyderabad, Kandi, Sangareddy, Telangana State-502284, India.*
** E-mail: narendra@chy.iith.ac.in (Corresponding author)*
†Electronic Supplementary Information (ESI)

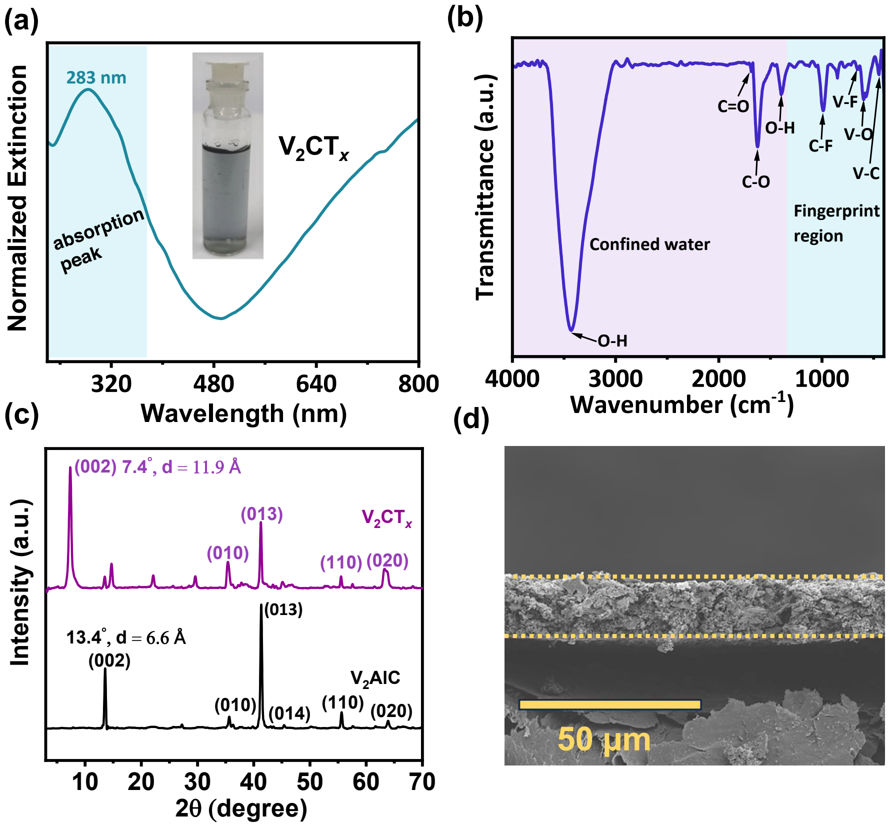

Fig. S1. Material characterization. (a) Ultraviolet-Visible-Near-Infrared (UV-Vis-NIR) spectrum of V_2CT_x MXene dispersed in deionized (DI) water, showing a characteristic absorption peak at 283 nm (inset showing the digital photograph of dispersed V_2CT_x in DI water). (b) Fourier transform infrared (FTIR) spectrum of V_2CT_x MXene. (c) X-ray diffraction (XRD) patterns of V_2AlC MAX phase (black) and V_2CT_x MXene (purple). (d) Field emission scanning electron microscopy (FESEM) image of V_2CT_x MXene electrode coated over graphite foil (cross-sectional view).

Optical absorption characteristics of V_2CT_x MXene was examined by recording an Ultraviolet-Visible-Near-Infrared (UV-Vis-NIR) spectrum after bath sonication. The characteristic absorption peak at 283 nm matches with the reported literature (as shown in Fig. S1a).[1] Fourier transform Infrared (FTIR) spectrum was recorded to identify the presence of functional groups, type of chemical bonding such as V-C, V-F, C-O, and V-O in the fingerprint region (1400-450 cm^{-1}), and confined water region (4000-1400 cm^{-1}) (Fig. S1b). To investigate the structural evolution of V_2CT_x MXene after etching from its MAX precursor, X-ray diffraction (XRD) pattern was recorded. The characteristic (002) peak of V_2AlC at 2θ ~ 13.4° with *d*-spacing of 6.6 Å was downshifted to 7.4° with an enlarged *d*-spacing of 11.9 Å in V_2CT_x MXene, which matches well with the reported literature.[1] The enlargement of the *d*-spacing is attributed to the selective extraction of Al atomic layers, followed by the introduction of surface functional groups such as =O, -OH, -F, and -Cl onto the V_2CT_x MXene during the etching process (Fig. S1c). Fig. S1d shows the cross-sectional view of uniform coating of the V_2CT_x MXene over a graphite foil current collector with a typical thickness of ~ 25 µm.

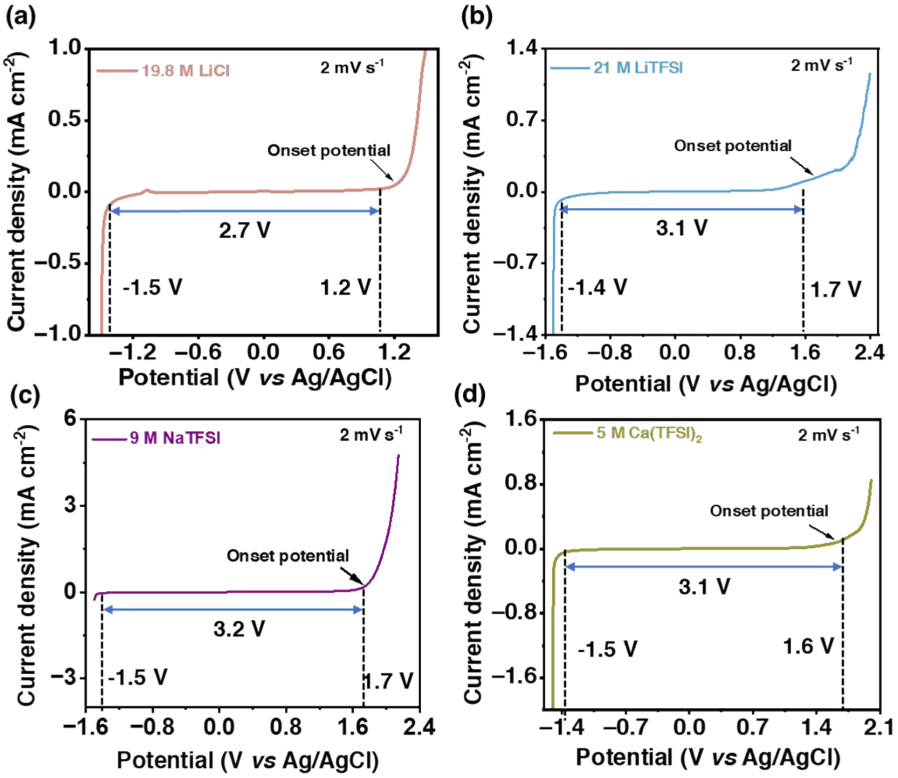

Fig. S2. Linear sweep voltammograms (LSVs) of (a) 19.8 M LiCl, (b) 21 M LiTFSI, (c) 9 M NaTFSI, (d) 5 M $Ca(TFSI)_2$ aqueous concentrated electrolytes, reflecting the electrochemical stability window (ESW) Water-in-Salt electrolytes (WiSE) employed in the current study.

To examine the electrochemical stability window (ESW) of WiSE such as 19.8 M LiCl, 21 M LiTFSI, 9 M NaTFSI, 5 M $Ca(TFSI)_2$, bare glassy carbon electrodes were employed as current collectors. Non-Faradaic processes are prevalent within the potential window of -1.5 V to 1.7 V *vs* Ag/AgCl, indicating that glassy carbon is passive and does not exhibit side reactions (Fig. S2). In almost all saturated electrolytes, ESW was found to be > 2.5 V (*vs* Ag/AgCl). The following ESW values are listed in the table S1.

Table S1. Electrochemical stability window of water-in-salt electrolytes (WiSE) are given below:

S. No.	**Electrolytes**	**ESW (V *vs* Ag/AgCl)**
1.	19 M LiCl	-1.5 to 1.2
2.	21 M LiTFSI	-1.5 to 1.7
3.	9 M NaTFSI	-1.5 to 1.7
4.	5 M $Ca(TFSI)_2$	-1.5 to 1.6

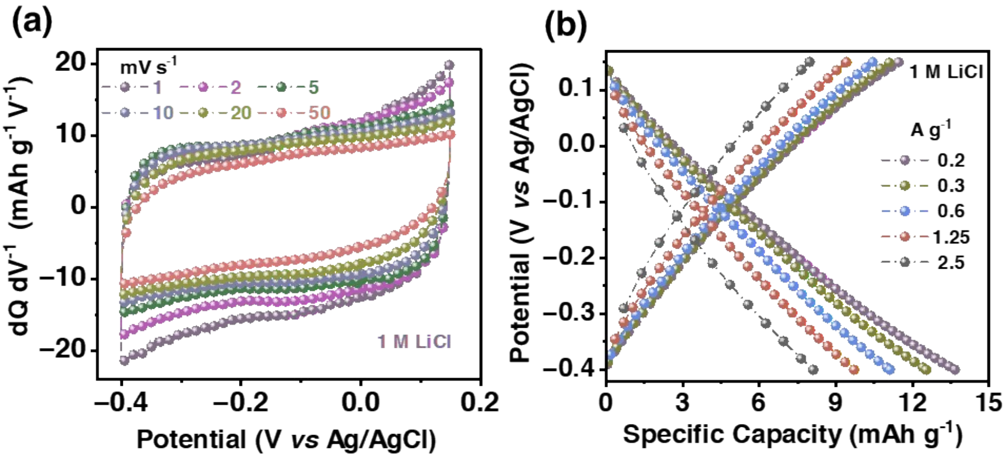

Fig. S3. (a) Cyclic voltammograms (CVs) of V_2CT_x MXene in 1 M LiCl aqueous electrolyte at various scan rates ranging from 1 to 50 mV s^{-1}. (b) Galvanostatic charge-discharge profiles of V_2CT_x MXene in 1 M LiCl electrolyte at different current densities from 0.2 to 2.5 A g^{-1}.

As shown in Fig. S3a, V_2CT_x MXene showed a capacitive behaviour in 1 M LiCl with a narrow potential window operation of -0.4 to 0.15 V (*vs* Ag/AgCl). CVs were recorded at various scan rates ranging from 1 to 50 mV s^{-1}. The narrow potential window of operation arises due to possible gas evolution or irreversible cathodic reduction reaction (ICRR) at cathodic potentials and irreversible anodic oxidation reaction (IAOR) of V_2CT_x at anodic potentials. Galvanostatic charge/discharge profiles were recorded at different current densities from 0.2 to 2.5 A g^{-1}. The specific capacity of V_2CT_x was found to be < 20 mAh g^{-1} at a current density of 0.2 A g^{-1} in 1 M LiCl electrolyte (Fig. S3b).[2]

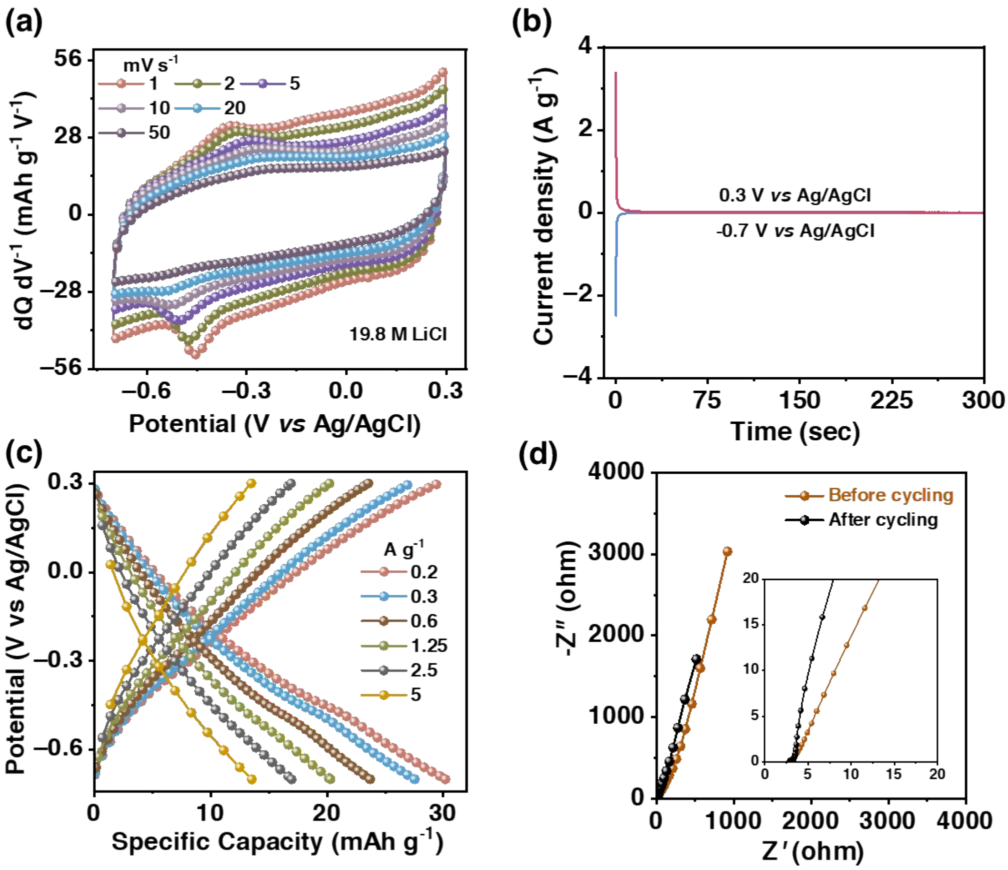

Fig. S4. (a) Cyclic voltammograms (CVs) of V_2CT_x MXene in 19.8 M LiCl aqueous electrolyte at various scan rates. (b) Chronoamperometry profiles at anodic and cathodic potentials in 19.8 M LiCl electrolytes. (c) Galvanostatic charge-discharge (GCD) profiles of V_2CT_x MXene in 19.8 M LiCl electrolyte at different current densities from 0.2 to 5 A g^{-1}. (d) Electrochemical impedance spectra (EIS) of V_2CT_x MXene in 19.8 M LiCl electrolyte before and after cycling test (inset showing the impedance spectra at high frequency region).

In the case of 19.8 M LiCl aqueous electrolyte, the anodic potential limit of the V_2CT_x MXene electrode is 0.3 V (*vs* Ag/AgCl). However, V_2CT_x MXene showed a pair of redox peaks at potentials of -0.35/-0.45 V (*vs* Ag/AgCl) (anodic/cathodic) at high concentration (Fig. S4a). The stable cut-off potentials were confirmed by chronoamperometry measurements (Fig. S4b). At 0.2 A g^{-1}, V_2CT_x MXene showed a sloping type of charge-discharge profile with a lithiation capacity of 32 mAh g^{-1} (Fig. S4c). To understand the impedance characteristics of V_2CT_x electrode |19.8 M LiCl WiSE interface, electrochemical impedance spectroscopy was recorded from high frequency (100 kHz) to low frequency (10 mHz) regime. At the high frequency regime, the equivalent series resistance (ESR) corresponding to the X-axis intercept was decreased from 3.6 to 2.8 Ω after cycling, which is possibly due to the better wettability of the electrolyte and facile diffusion of ions after cycling (Fig. S4d).

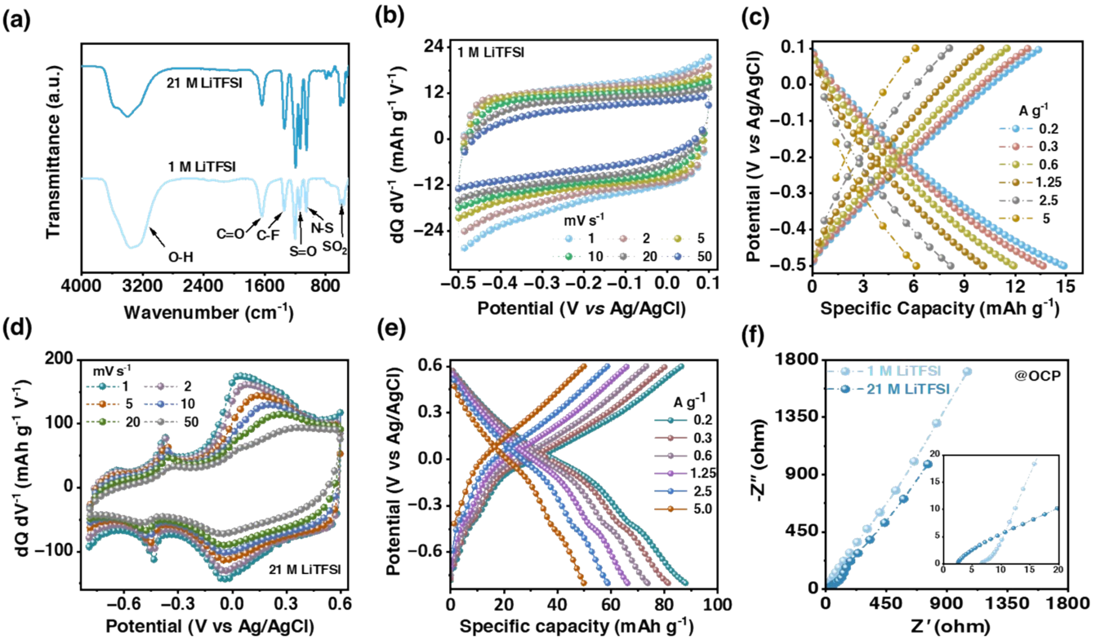

Fig. S5. Electrochemical performance of V_2CT_x MXene in different concentrations of LiTFSI aqueous electrolytes. (a) Attenuated total reflectance Fourier transform infrared (ATR-FTIR) spectra of 1 and 21 M LiTFSI aqueous electrolytes. (b) CVs of V_2CT_x MXene at different scan rates range from 1 to 50 mV s^{-1} in 1 M LiTFSI aqueous electrolyte. (c) GCD profiles of V_2CT_x MXene in 1 M LiTFSI aqueous electrolyte at various current densities ranging from 0.2 to 5 A g^{-1}. (d) CVs of V_2CT_x MXene in 21 M LiTFSI aqueous electrolyte at different scan rates, from 1 to 50 mV s^{-1}. (e) GCD profiles of V_2CT_x MXene in 21M LiTFSI aqueous electrolyte at various current densities ranging from 0.2 to 5 A g^{-1}. (f) Electrochemical impedance spectra (EIS) of V_2CT_x MXene in 1 and 21 M LiTFSI aqueous electrolytes at open circuit potential condition, 0.2 V vs. Ag/AgCl (inset showing the impedance spectra at high frequency region).

Attenuated total reflectance Fourier transform infrared (ATR-FTIR) spectroscopy was employed to investigate the evolution of water coordination as a function of increasing concentration of LiTFSI electrolyte from 1 to 21 M. ATR-FTIR spectra of 1 and 21 M LiTFSI aqueous electrolytes are shown in Fig. S5a, where a broad and intense absorption peak appears in the range of 3000-3600 cm^{-1} which corresponds to the O-H stretching vibrations of H_2O molecules. Similarly, the absorption peaks at 1636, 1344, 1203, and 1050 cm^{-1} correspond to C=O, C-F, S=O and N-S stretching vibrations, whereas the peak around 579 cm^{-1} corresponds to SO_2 bending vibration of the TFSI anion.[3] With an increase in concentration from 1 M to 21 M LiTFSI, the absorption intensity of the O-H (3000-3600 cm^{-1}) stretching vibration decreases, and the absorption intensity of the TFSI ion increases, signifying the less availability of free water molecules in water-in-salt (WiS) electrolytes. Thus, in WiS electrolytes, the coordination of H_2O molecules per ion decreases compared to that of dilute (1 M) electrolytes.[4]

V_2CT_x MXene showed a capacitive behaviour in 1 M LiTFSI electrolyte with limited lithiation capacity of 15 mA h g^{-1} at a current density of 0.2 A g^{-1}, typically due to intercalation of hydrated Li^+ ions into 2D galleries of MXene (Fig. S5b-5c). In contrast, V_2CT_x MXene showed a pair of redox peaks at -0.37/-0.43 V (*vs* Ag/AgCl) in 21 M LiTFSI aqueous electrolyte, similar to that of 19.8 M LiCl electrolyte. Notably, an additional broad redox envelop from -0.2 to 0.3 (*vs* Ag/AgCl) was observed. It was reported that the hydrogen-bonding state of confined water between the interlayers of $Ti_3C_2T_x$ changes with increasing ion concentration. Fundamentally, two different types of Li-ion insertion mechanisms were proposed: a capacitive-type mechanism due to the intercalation of hydrated cations at cathodic potentials and redox type at anodic potentials due to desolvation-free Li-ion (de)intercalation. Given the difference in the redox behavior of vanadium (V) compared to titanium (Ti), it is expected that the interaction of ions with V_2CT_x could be different from the previous work on WiSE in $Ti_3C_2T_x$ MXene.[5] The pairs of redox peaks within the tested potential range suggest the participation of partially unfilled 3d orbital of V^{4+} in V_2CT_x and M^{n+} ion, consistent with previous reports. [6, 7]

The **standard reduction potentials (E^0)** of the vanadium redox couples in acidic aqueous solution (typically 1 M H^+, 25 °C) *vs* **SHE are** shown below:

$$V^{3+} + e^- \rightleftharpoons V^{2+}$$

$$E^0_{V^{3+}/V^{2+}} \approx \mathbf{-0.255\ V}\ \mathit{vs}\ \mathbf{SHE\ or\ -0.45\ V\ (}\mathit{vs}\ \mathbf{Ag/AgCl)}$$

V^{4+}/V^{3+} (commonly written as VO^{2+}/V^{3+} in acid)

$$VO^{2+} + 2H^+ + e^- \rightleftharpoons V^{3+} + H_2O$$

$$E^0_{V^{4+}/V^{3+}} \approx \mathbf{+0.34\ V}\ \mathit{vs}\ \mathbf{SHE\ or\ +0.14\ V\ (}\mathit{vs}\ \mathbf{Ag/AgCl)}$$

As shown in Fig. S5d, the CVs exhibited redox peaks at -0.5 V (*vs* Ag/AgCl) and 0 V (*vs* Ag/AgCl) corresponding to V^{3+}/V^{2+} and V^{4+}/V^{3+} redox couples, respectively. This clearly signifies the redox-active nature of the V^{4+} component, and the broad peaks are attributed to the inhomogeneous surface terminations due to the random distribution of functional groups.

Due to additional redox capacity at the extended potential window (> 0 V *vs* Ag/AgCl), the lithiation capacity of V_2CT_x MXene was found to be 90 mAh g^{-1} at a current density of 0.2 A g^{-1} (Fig. S5e). To understand the charge transfer kinetics, electrochemical impedance spectroscopy was recorded from high frequency (100 kHz) to low frequency (10 mHz) region at the open circuit potential (OCP) condition. At the high frequency regime, the equivalent series resistance (ESR) corresponding to the X-axis intercept was found to be 6.6 and 2.4 Ω for 1 M and 21 M LiTFSI electrolytes, respectively. The low ESR value at high concentration is possibly due to increased number of charge carriers at high concentration with reduced ion pairing due to the weak coordination environment. In the case of 21 M LiTFSI electrolyte, 45° line (Warburg diffusion, corresponding to solid state diffusion) is prevalent in the moderate frequency regime, unlike the case of 1 M electrolyte (Fig. S5f).

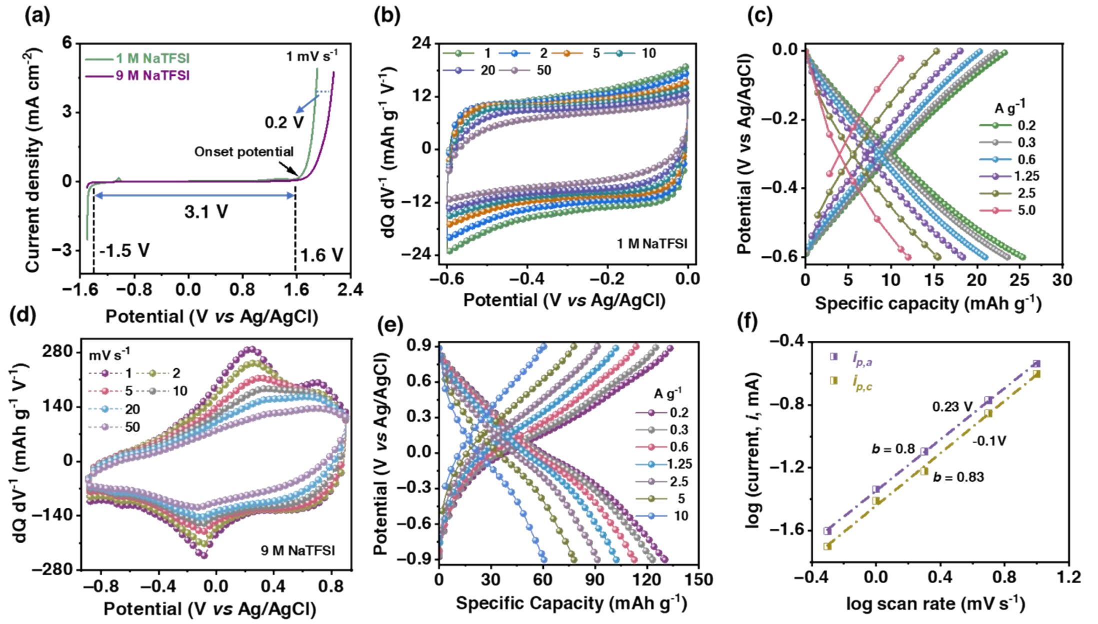

Fig. S6: (a) Linear sweep voltammograms (LSVs) of 1 M and 9 M NaTFSI aqueous electrolytes at a scan rate of 1 mV s^{-1}. (b) CVs of V_2CT_x MXene in 1 M NaTFSI aqueous electrolytes at various scan rates ranging from 1 to 50 mV s^{-1}. (c) GCD profiles of V_2CT_x MXene in 1 M NaTFSI electrolyte at different current densities from 0.2 to 5 A g^{-1}. (d) CVs of V_2CT_x MXene in 9 M NaTFSI electrolyte at scan rates ranging from 1 to 50 mV s^{-1}. (e) GCD profiles at different current densities from 0.2 to 10 A g^{-1}. (f) Kinetic parameter, *b*-value, obtained from the slope of log (current) *vs* log (scan rate) plot at applied potentials of 0.23 V and -0.1 V vs. Ag/AgCl, corresponding to anodic and cathodic sweeps, respectively.

To examine the electrochemical stability window (ESW) of electrolytes, bare glassy carbon electrodes were employed as current collectors. Non-Faradaic processes are prevalent in the potential window of -1.5 V to 1.6 V, signifying that glassy carbon is passive without exhibiting side reactions with a typical ESW of 3.1 V (*vs* Ag/AgCl). At a saturated concentration of 9 M, the onset potential for the irreversible anodic oxidation reaction (IAOR) is observed at an additional overpotential of 0.2 V in comparison to dilute electrolyte (Fig. S6a). As shown in Fig. S6b, V_2CT_x MXene showed capacitive behavior in 1 M NaTFSI electrolyte with a narrow potential window operation of -0.6 to 0 V (*vs* Ag/AgCl). On the contrary, when the concentration of salt was increased from 1 to 9 M, V_2CT_x MXene electrode exhibited reversible redox electrochemistry in the case of 9 M NaTFSI, plausibly due to less availability of free water around the cations and weak coordination of asymmetric TFSI$^-$ anions, which helps in fast transport of partially hydrated cations. Increasing the salt concentration up to 9 M results in an unusually wide potential window of -0.9 to 0.9 V (*vs* Ag/AgCl) with a pair of reversible redox peaks at ~ 0.23/-0.08 V (*vs* Ag/AgCl) and an additional oxidation peak at 0.7 V (*vs* Ag/AgCl) which is plausibly due to change in oxidation state of V^{3+} to V^{4+} in the V_2CT_x (Fig. S6d). The presence of anodic peaks and a corresponding cathodic peak corresponds to the redox-type charge storage of Na^+ ions into V_2CT_x MXene. A similar kind of behaviour was observed in $Ti_3C_2T_x$ MXene in a 19.8 m LiBr electrolyte.[8]

Furthermore, galvanostatic charge/discharge (GCD) profile of V_2CT_x MXene was performed in 9 M NaTFSI electrolyte at different current densities from 0.2 to 10 A g^{-1}. The increase in salt concentration results in an enhancement of the specific capacity up to five-fold compared to that of dilute 1 M NaTFSI (< 30 A g^{-1}) (Fig. S6c and 6e). V_2CT_x MXene showed a sodiation capacity of 131 mAh g^{-1} at a current density of 0.2 A g^{-1} in 9 M NaTFSI and even at high current density of 10 A g^{-1}, the electrode retained a sodiation capacity of 46 %, indicating the better charge storage capability of the electrode in WiS sodium-ion electrolyte. Therefore, the redox peaks that appear in the anodic potential contribute to the sodiation storage capacity of V_2CT_x MXene in 9 M NaTFSI.

The electrochemical kinetics of Na-ions across the V_2CT_x electrode were investigated by employing the power law relationship between current response (i, mA) and scan rate (ν, mV s^{-1}) as shown in equations 3 and 4 (see experimental section). The slope (b-value) provides information about surface-controlled and diffusion-controlled kinetics. When the b-value is 0.5, the process is diffusion-controlled. Similarly, the b-value corresponds to 1 signifies the surface-controlled process. The estimated b-values at potentials of 0.23 and -0.1 V (*vs* Ag/AgCl) were 0.8 and 0.83, respectively, indicating the dominance of surface-controlled over diffusion-controlled kinetics (Fig. S6f).

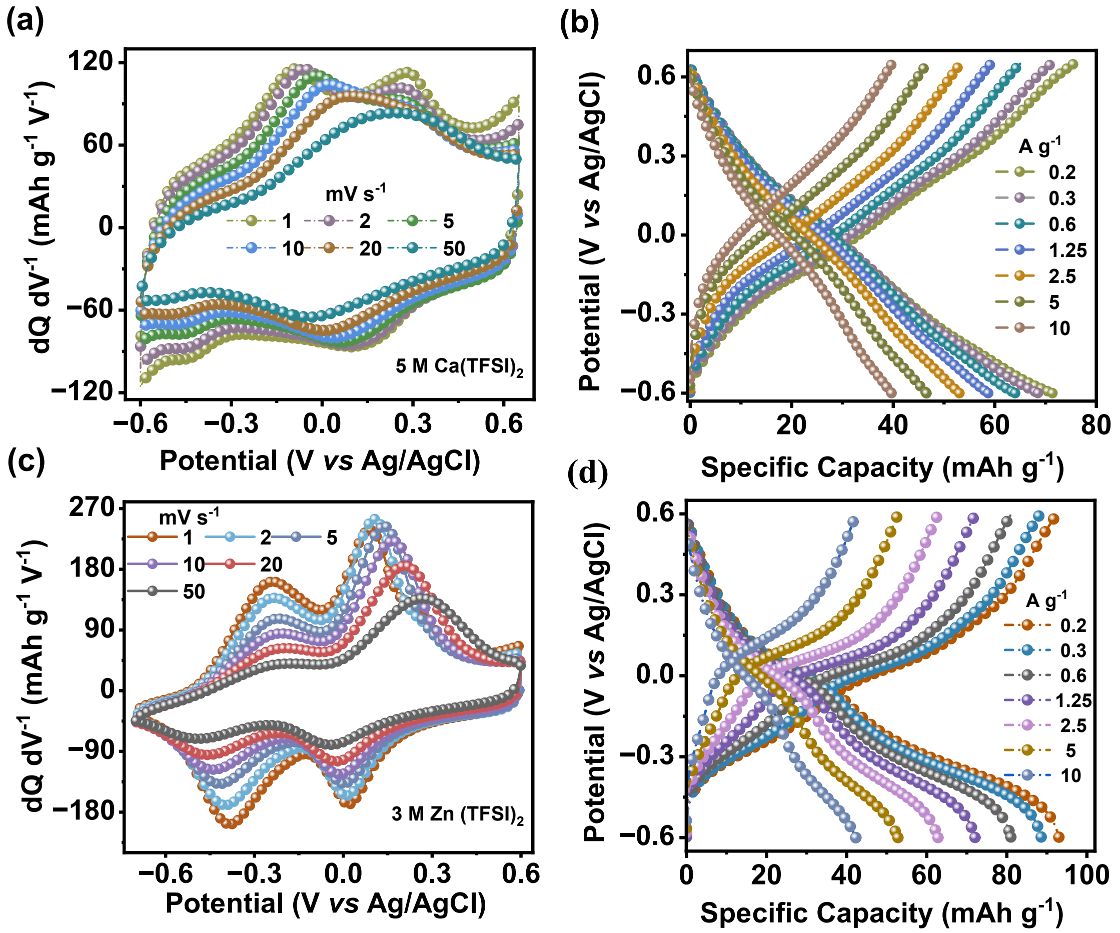

Fig. S7. (a) Cyclic voltammograms (CVs) of V_2CT_x MXene in 5 M Ca(TFSI)$_2$ aqueous electrolyte at various scan rates from 1 to 50 mV s^{-1}. (b) Galvanostatic charge-discharge (GCD) profiles of V_2CT_x MXene in 5 M Ca(TFSI)$_2$ electrolytes at different current densities from 0.2 to 10 A g^{-1}. (c) CVs of V_2CT_x MXene in 3 M Zn(TFSI)$_2$ aqueous electrolyte at various scan rates from 1 to 50 mV s^{-1}. (d) GCD profiles of V_2CT_x MXene in 3 M Zn(TFSI)$_2$ electrolytes at different current densities from 0.2 to 10 A g^{-1}.

At a high concentration of 5 M Ca(TFSI)$_2$, V_2CT_x MXene showed an extended operational potential window of -0.6 to 0.7 V (*vs* Ag/AgCl). CVs were recorded at different scan rates ranging from 1 to 50 mV s^{-1} (Fig. S7a). The electrode showed a pair of anodic peaks at -0.1 and 0.28 V (*vs* Ag/AgCl) across anodic potential and a corresponding broad cathodic peak at 0.12 V (*vs* Ag/AgCl). Typical sloping type charge-discharge profiles are evident in 5 M Ca(TFSI)$_2$

electrolyte. GCD profiles were recorded at different current densities of 0.2 to 10 A g^{-1}, where V_2CT_x MXene showed a calciation capacity of 72 mAh g^{-1} at a current density of 0.2 A g^{-1} (Fig. S7b).

At a high concentration of 3 M $Zn(TFSI)_2$, V_2CT_x MXene showed an extended operational potential window of -0.7 to 0.6 V *vs* Ag/AgCl. CVs were recorded at different scan rates from 1 to 50 mV s^{-1} (Fig. S7c). The electrode showed two pairs of reversible redox peaks at -0.25/-0.38 and 0.1/0.02 V (*vs* Ag/AgCl), possibly due to the change in oxidation state from V^{2+}/V^{3+} and $V^{3+/}V^{4+}$, respectively. V_2CT_x showed typical sloping type charge-discharge profiles in 3 M $Zn(TFSI)_2$ electrolyte. GCD profiles were recorded at different current densities of 0.2 to 10 A g^{-1}, where V_2CT_x MXene showed a zincification capacity of 90 mAh g^{-1} at a low current density of 0.2 A g^{-1} (Fig. S7d).

Theoritical specific capacity is given by the formula:

$$C\ (mAh\ g^{-1}) = \frac{nF}{3.6\ MW} \qquad \text{(Eq. S1)}$$

where F represents the Faraday constant (96500 C/mol), *n* is the number of electrons transferred, and MW stands for the molecular weight of V_2CO_2 (145.89 g mol^{-1}). As we observe broad redox peaks in the CV curves, partial charge transfer is occurring between V_2CO_2 and Li^+, Na^+, Ca^{2+}, and Zn^{2+} ions. The proposed redox mechanism between MXene and metal-ions is given by the following general reversible reaction:

$$V_2CO_2 + xM^{n+} + nxe^- \rightarrow M_xV_2CO_2$$

where $M^{n+} = Li^+$, Na^+, Ca^{2+}, and Zn^{2+}

The practical capacity of V_2CO_2 MXene in 21 M LiTFSI electrolyte is 90 mAh g^{-1}, and the '*n*' value is found to be 0.5. Based on this, the electrochemical reaction can be written as

$$V_2CO_2 + 0.5Li^+ + 0.5e^- \rightarrow Li_{0.5}V_2CO_2$$

Such a discrepancy in the practical charge storage capacity is possibly attributed to inhomogeneous and inactive surface terminations (-OH, -F).

Similarly, the *n* values were found to be 0.7, 0.4, and 0.5 for 9 M NaTFSI, 5 M $Ca(TFSI)_2$, and 3 M $Zn(TFSI)_2$ electrolytes, respectively. The electrochemical reaction could be written as:

$$V_2CO_2 + 0.7Na^+ + 0.7e^- \rightarrow Na_{0.7}V_2CO_2$$
$$V_2CO_2 + 0.4Ca^{2+} + 0.8e^- \rightarrow Ca_{0.4}V_2CO_2$$
$$V_2CO_2 + 0.5Zn^{2+} + 1.0e^- \rightarrow Zn_{0.5}V_2CO_2$$

Practically, the charge species that are responsible for observed capacity may not be the same as mentioned above. Specifically, divalent metal cations tend to form complex ionic species such as $[MTFSI]^+$ and co-solvent species. Thus, electrochemical quartz crystal microbalance studies may be required to investigate the nature of ionic species involved in storing across the interlayer spaces of V_2CT_x MXene.

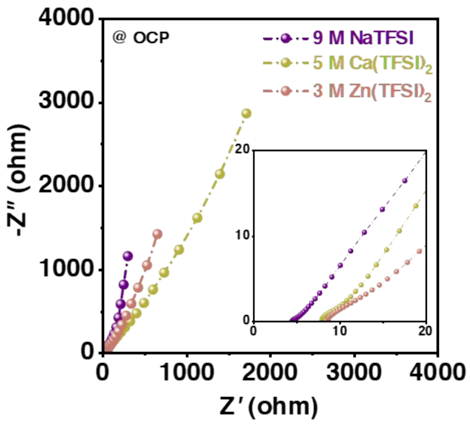

Fig. S8. Nyquist impedance spectra of V_2CT_x MXene electrode in 9 M NaTFSI, 5 M $Ca(TFSI)_2$, and 3 M $Zn(TFSI)_2$ electrolytes at open circuit potential (OCP) conditions.

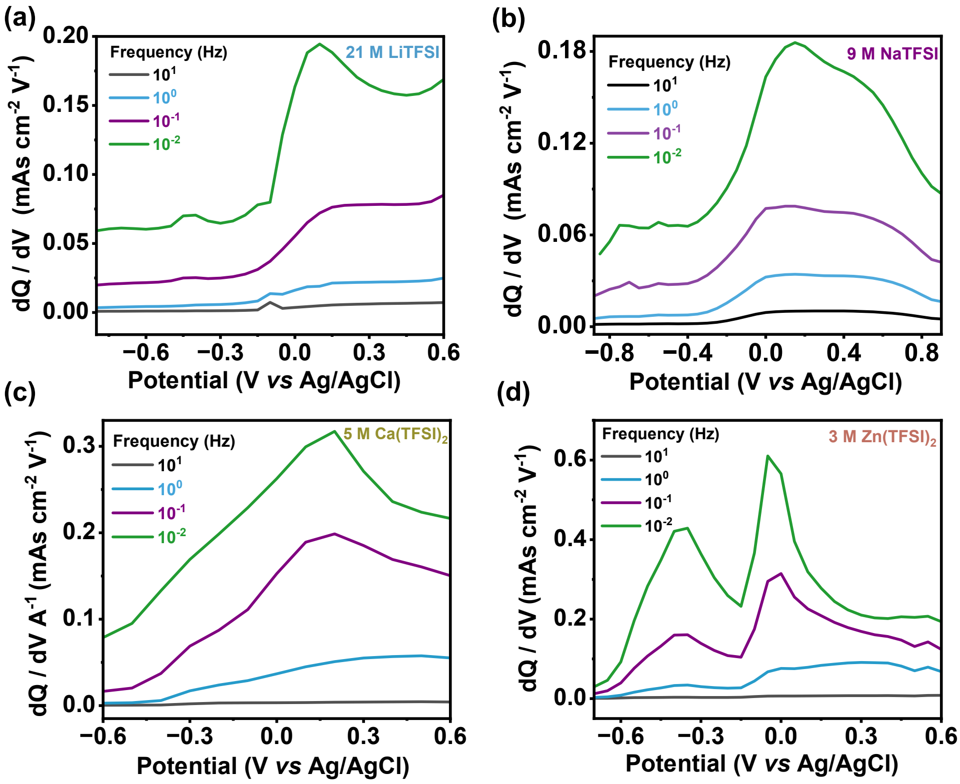

Fig. S9. 2D Bode plots representing differential areal capacity of V_2CT_x MXene electrode as a function of potential ($\left(\frac{dQ}{dV}\right)$, *vs* Ag/AgCl at different frequencies (Hz) in (a) 21 M LiTFSI, (b) 9 M NaTFSI, (c) 5 M $Ca(TFSI)_2$, (d) 3 M Zn $(TFSI)_2$ saturated electrolytes.

It is evident from 2D Bode plots that redox behaviour of the V_2CT_x electrode over a potential range of -0.9 to 0.9 V (*vs* Ag/AgCl) in saturated electrolytes (Fig. S9) in the low frequency regime (10, 1, 01, 0.01 Hz).

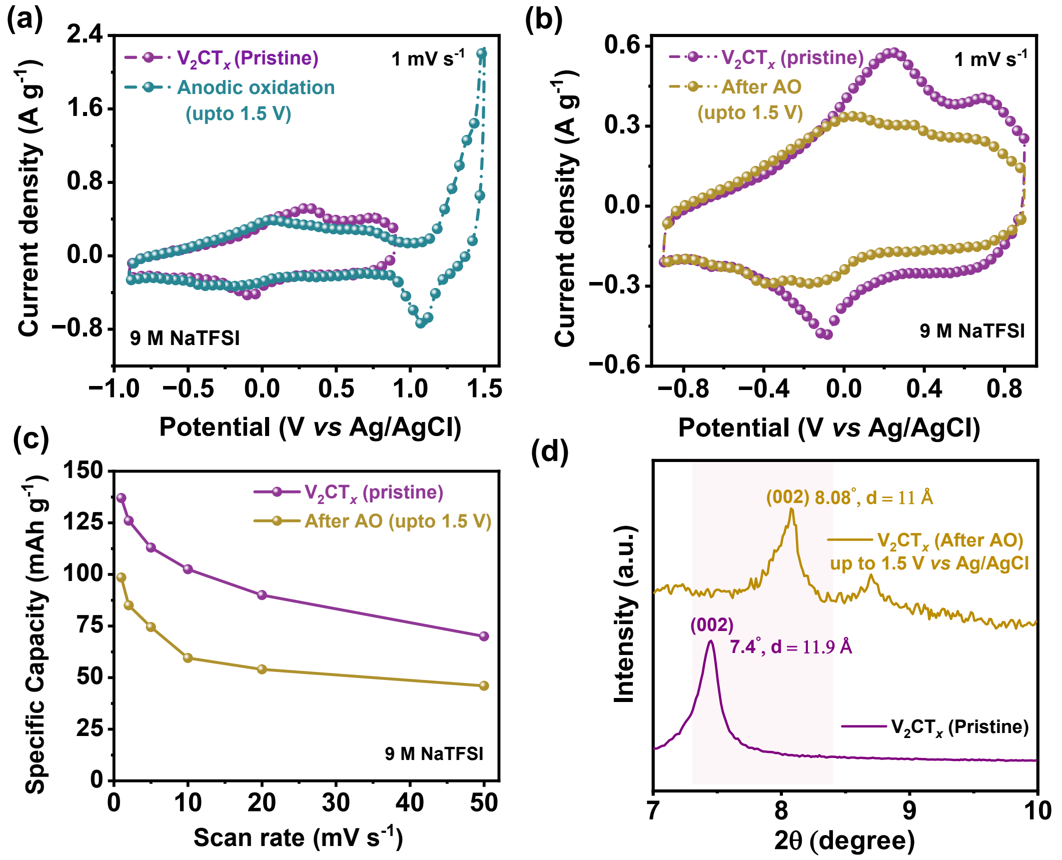

Fig. S10. Electrochemical behavior of the V_2CT_x MXene electrode in 9 M NaTFSI electrolyte before and after anodic oxidation up to 1.5 V (*vs* Ag/AgCl) at a scan rate of 1 mV s^{-1}. (a) Comparative cyclic voltammograms (CVs) of V_2CT_x MXene within the stable operational window and anodically oxidized window at a scan rate of 1 mV s^{-1}. (b) Comparative CVs of pristine, anodically oxidized V_2CT_x MXene at a scan rate of 1 mV s^{-1}. (c) Specific capacity as a function of scan rate plot for pristine and anodically oxidized V_2CT_x MXene. (d) X-ray diffraction (XRD) patterns of pristine (purple) and anodically oxidized V_2CT_x MXene (yellow) electrode.

To investigate the intrinsic redox behaviour of V_2CT_x, in-situ anodic oxidation was performed by oxidizing V_2CT_x MXene in 9 M NaTFSI WiS electrolyte between the potential range of -0.9 to 1.5 V (*vs* Ag/AgCl) at a scan rate of 1 mV s^{-1} for ~ 10 sweeps (Fig. S10a). It was noticed that, with subsequent cycling for more than 10 CV cycles, the area under the CV curve diminished and overall specific capacity decreased (Fig. S10b). After anodic oxidation up to 1.5 V (*vs* Ag/AgCl), the specific capacity reduced to 100 mAh g^{-1} at a scan rate of 1 mV s^{-1}, which is a 24% reduction in the capacity value (Fig. S10c). This reduction in sodiation capacity is possibly attributed to the saturation of the redox-active valence states of vanadium. This particular experiment clearly demonstrates that irreversible anodic oxidation is the main event at anodic potentials rather than oxygen evolution reaction (OER). This is also in agreement with previous report on subjecting V_2CT_x to partial anodic oxidation and extreme anodic oxidation in the concentrated electrolytes.[7] Electrochemical kinetics of storage of ions improved while partial oxidation and CV became completely resistive after being subjected to extreme anodic oxidation.[7] On the contrary, if at all the electrocatalytic nature of V_2CT_x is operating at anodic potentials, the electrochemical nature of the electrode should remain unaltered during the oxygen evolution reaction. Moreover, OER should lead to expansion of V_2CT_x layers due to local evolution of gas and that supposed to increase the electrochemical active surface area and hence should improve the charge storage capacity. To understand the structural changes after biasing the electrode to a high anodic potential, X-ray diffraction (XRD) was performed on both the pristine and the electrode after anodic oxidation (AO).

From the XRD pattern, it was found that, V_2CT_x MXene experienced anodic oxidation, which possibly formed VO_x oxides upon reaction with water, leading to a reduction in the active surface area of the electrode. Pristine MXene electrode showed a typical d-spacing of 11.9 Å, whereas the electrode after AO showed a d-spacing of 11Å, which is a 0.9 Å reduction compared to the pristine electrode (Fig. S10d).

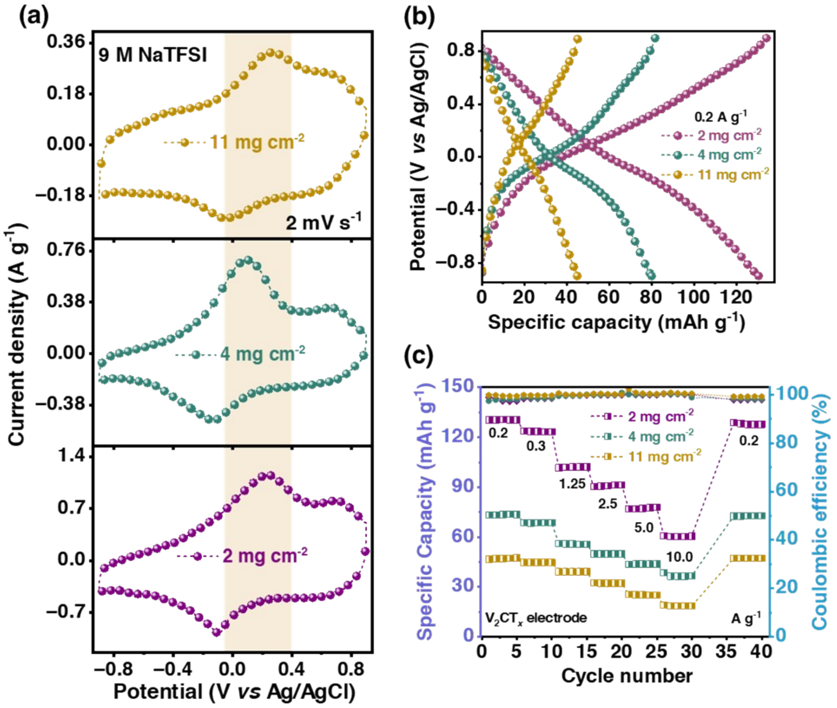

Fig. S11. Electrochemical performances of V_2CT_x MXene in 9 M NaTFSI at various mass loadings (2, 4, 11 mg cm^{-2}). (a) Cyclic Voltammograms of V_2CT_x MXene at different mass loadings at a scan rate of 2 mV s^{-1}. (b) Galvanostatic charge-discharge at a current density of 0.2 A g^{-1}. (c) Comparison of rate performance of V_2CT_x MXene (at different mass loadings) at various current densities from 0.2 to 10 A g^{-1}.

Further, to evaluate the effect of areal mass loadings of V_2CT_x MXene (2 mg cm^{-2}, 4 mg cm^{-2} and 11 mg cm^{-2}) in 9 M NaTFSI WiSE, electrochemical measurements were performed. As shown in Fig. S1a, the signature electrochemical characteristics of V_2CT_x MXene in 9M NaTFSI electrolyte is well maintained at maximum mass loading of 11 mg cm^{-2} (refer to CVs at a scan rate of 2 mV s^{-1}). As expected, the sodiation capacity of V_2CT_x MXene reduced to ~ 37% at high mass loading (~ 11 mg cm^{-2}) in comparison to moderate mass loading of 2 mg cm^{-2} (Fig. S11b). Such kind of reduction in the electrochemical performance with increasing mass loading is attributed to the restacking of layered materials, causing inaccessibility to the electrochemical active sites.[9] Such a reduction in electrochemical performance is the main challenge in delivering specific capacities in line with increased thickness of electrode, where the electrode showed a good rate capability in all the taken mass loadings (Fig. S11c). However, it was reported that liquid crystalline aligned $Ti_3C_2T_X$ MXene showed thickness independent.[10] Possibly, such kind of electrode architectures may be developed in order to maintain the electrochemical performance at high mass loadings.

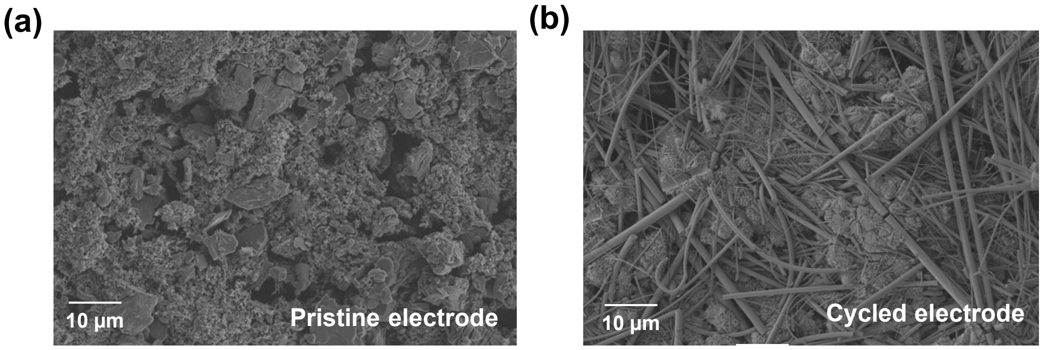

Fig. S12. FESEM images of V_2CT_x (a) pristine and (b) cycled electrode.

To check the morphological changes of V_2CT_x MXene over 10,000 charge-discharge cycles in 9 M NaTFSI WiSE, FESEM images were recorded for both pristine and cycled electrodes. In the case of pristine electrode, V_2CT_x MXene is uniformly distributed throughout the electrode surface along with the binder and conductive additive (Fig. S12a). After the cycling stability test over 10,000 cycles, the electrode is well preserved, but some of the glass microfibres from the separator were deposited over the electrode surface (Fig. S12b).

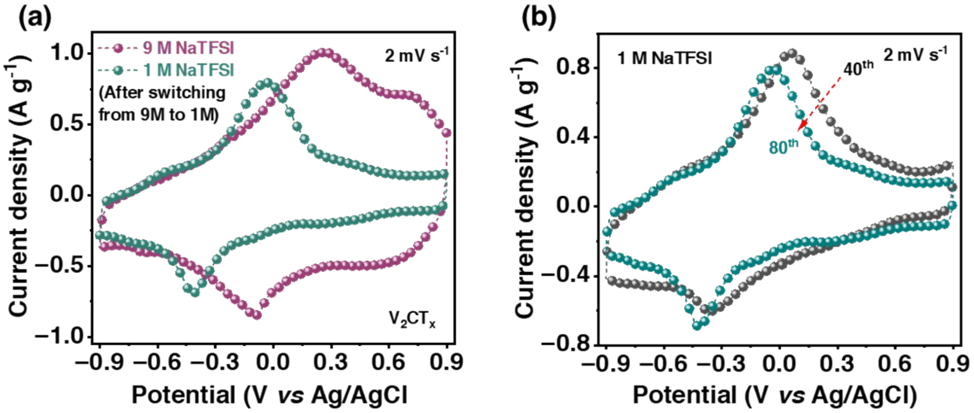

Fig. S13. (a) Comparative cyclic voltammograms of the V_2CT_x MXene electrode in 9 M NaTFSI electrolyte and after switching to 1 M NaTFSI at a scan rate of 2 mV s^{-1}. (b) CVs reflecting reduction in the current response in 1 M NaTFSI over the cycles at a scan rate of 2 mV s^{-1}.

To understand the electrochemical behaviour of V_2CT_x MXene in the anodic potential window in dilute medium, the electrode containing 9 M NaTFSI was swicthed to dilute (1 M NaTFSI). (i) When 1M NaTFSI electrolyte was employed, the stable electrochemical window is found to be -0.6 V to 0.1 V *vs* Ag/AgCl. At this concentration, upon expanding the potential window beyond 0.2 V *vs* Ag/AgCl, a sudden rise in the current value was observed, which is attributed to irreversible anodic oxidation. (ii) However, such kind of irreversible anodic oxidation was suppressed when using 9M NaTFSI aqueous electrolyte. Rather, we observed reversible redox chemistry of V^{3+}/V^{4+} redox couple at potentials of 0.25 and 0.7 V *vs* Ag/AgCl and corresponding reduction peak at -0.1 V *vs* Ag/AgCl. (iii) After running the electrochemical cell in 9M NaTFSI electrolyte, 1 M NaTFSI electrolyte was employed by having same V_2CT_x MXene as working electrode that was tested in the concentrated electrolyte. An electrochemical stable window of -0.9 V to 0.9 V *vs* Ag/AgCl was observed, however, the redox peak corresponding to V^{3+}/V^{4+} was not observed (Fig. S13a). Most importantly, typical capacity decay of 2% per cycle is observed. Therefore, dynamic local environment across V_2CT_x MXene/concentrated electrolyte interface is different from dilute electrolyte interface. Thus, non-SEI formation is the primary reason for the unusual redox chemistry of V_2CT_x MXene in anodic potentials. In dilute medium, capacity fading is very rapid after subjecting the V_2CT_x electrode to anodic potential beyond 0.2 V *vs* Ag/AgCl. However, when switching from concentrated to dilute medium, capacity fading of V_2CT_x MXene is not rapid even after operating in the anodic potential window. This is possibly due to surface coverage of salt on V_2CT_x MXene in the highly concentrated medium, rather than permanent formation of stable SEI layer (Fig. S13b).

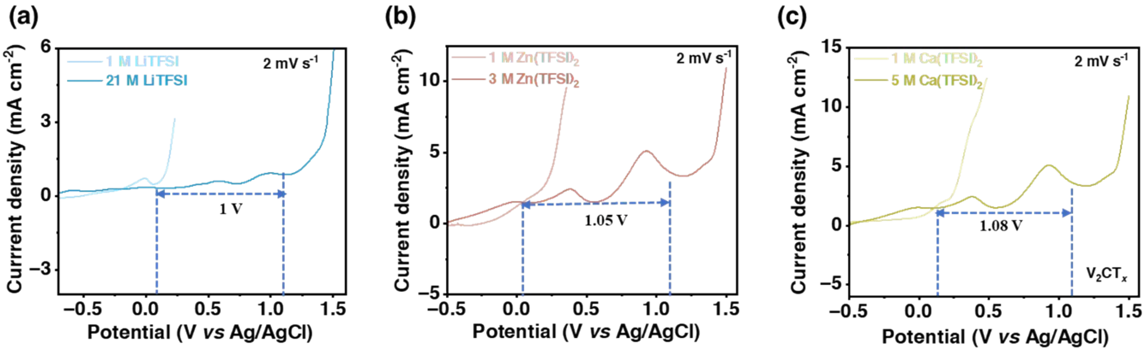

Fig. S14. Mechanism of electrochemical kinetics analysis of V_2CT_x MXene electrochemical interfaces. Current density (mA cm^{-2}) *vs* potential (V *vs* Ag/AgCl) plots showing the irreversible anodic oxidation of V_2CT_x electrode in both dilute and WiS electrolyte. (a) 1 and 21 M LiTFSI, (b) 1 and 3 M $Zn(TFSI)_2$, and (c) 1 and 5 M $Ca(TFSI)_2$.

Linear sweep voltammograms were recorded for all the dilute and concentrated electrolytes to understand the electrochemical kinetics over thermodynamic decomposition of water. The difference between the onset potentials of dilute and concentrated electrolytes was found to be 1, 1.05, and 1.08 V (*vs* Ag/AgCl) in LiTFSI, $Zn(TFSI)_2$, and $Ca(TFSI)_2$ electrolytes, respectively (Fig. S14). Due to water activity in dilute electrolytes, a rapid IAOR was observed. Whereas, due to the supressed water activity, sluggish IAOR kinetics was observed in the case of concentrated electrolytes, which means more overpotential is required to achieve desired current density.

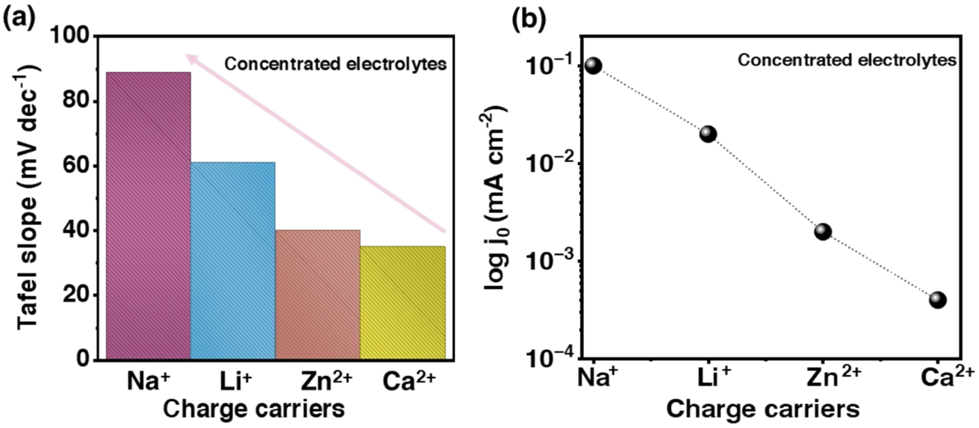

Fig. S15. Tafel analysis of various ionic charge carriers. (a) Trend of Tafel slope of various charge carriers of concentrated electrolytes (9 M NaTFSI, 21 M LiTFSI, 5 M $Ca(TFSI)_2$, 3 M $Zn(TFSI)_2$). (b) Trend of exchange current density (j_0, mA cm^{-2}) of different charge carriers.

In this context, the Tafel slope corresponds to the sensitivity of the rate of irreversible anodic oxidation (IAOR) to a change in the overpotential. It corresponds to determining the increase in the overpotential for a tenfold increase in current value for IAOR. The exchange current density (j_0) in this context corresponds to rate of charge transfer under equilibrium conditions.

At high salt concentrations, enhanced anodic stability is due to prominent interionic interactions along with association of water molecules, which result in sluggish reaction kinetics. As a result, we observe a delay in the irreversible anodic oxidation reaction (IAOR) at such highly concentrated electrolytes compared to their dilute counterparts. Among the charge carriers, Na^+ showed an expanded potential window of -0.9 to 0.9 V (*vs* Ag/AgCl) with a pair of redox peak corresponds to V^{3+}/V^{4+} redox couple, which was justified by Tafel analysis with a higher Tafel slope value of ~ 89 mV dec^{-1}. As Tafel slope depends upon the nature of the ions, and it is a dynamic situation under which the disturbance of tetrahedral water network occurs under applied potential. Due to the plausible complex formation of divalent ions (e.g., $CaTFSI^+$, $ZnTFSI^+$), the hydration shell might be easily deformed and can initiate reaction with the MXene surface at early onset potentials, compared to hydrated monovalent ions. Due to this, less overpotential is required to cause irreversible oxidation of the V_2CT_x MXene electrode in the case of divalent ions (Fig. S15a).

Further, among all four concentrated electrolytes (Li^+, Na^+, Zn^{2+}, and Ca^{2+}), Ca^{2+} showed the lowest exchange current density (j_0) value of $4*10^{-4}$ mA cm^{-2} due to high enthalpy of hydration and high charge density. Na^+ showed a comparatively higher j_0 (0.1 mA cm^{-2}) due to larger hydrated cation size and low enthalpy of hydration. Although the size of Zn^{2+} is smaller than that of Ca^{2+}, it has more favourable redox kinetics than Ca^{2+}, facilitating faster electron transfer, and slightly higher j_0 ($2*10^{-3}$ mA cm^{-2}). Similarly, due to the smaller size and high hydration enthalpy of Li^+, it showed a lower j_0 value (0.02 mA cm^{-2}) than Na^+ ion (Fig. S15b).

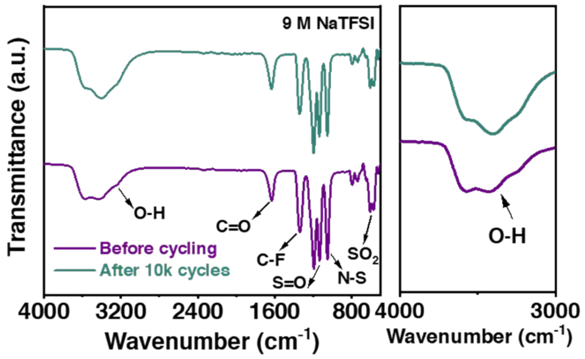

Fig. S16. Attenuated total reflectance Fourier transform infrared (ATR-FTIR) spectra of 9 M NaTFSI aqueous electrolyte before and after cycling test, and the magnified view showing O-H stretching vibration (3800 to 3000 cm^{-1}).

After cycling stability test over 10,000 cycles, the electrolytes were collected from the symmetric cell and the characteristics of 9 M NaTFSI aqueous electrolyte were investigated using attenuated total reflectance Fourier transform infrared (ATR-FTIR) spectroscopy. The characteristic O-H stretching and fingerprint regions of the electrolyte remain unaffected after the cycling test (Fig. S16). This indicates that there is hardly any modification in the concentrated electrolyte after cycling of the V_2CT_x //V_2CT_x symmetric cell.

Table S2. Electrochemical performances of reported electrode materials for water-in-salt (WiS) electrolytes.

Working electrode	**Electrolyte**	**Potential (V *vs* Ag/AgCl)**	**Specific Capacity (mAh g^{-1})**	**Mechanism**	**Ref.**
$NaMn[Fe(CN)_6]$	17M $NaClO_4$	0.0 to 1.3 V (*vs* Ag/AgCl)	130 @ 2 mA cm^{-2}	Non-SEI (sluggish IAOR)	11
$Ti_3C_2T_x$	3M H_2SO_4 + 10 M LiCl	-0.6 to 0.5 V (*vs* Ag/AgCl)	277 F g^{-1} @2 mV s^{-1}	Non-SEI (sluggish IAOR)	12
$Ti_3C_2T_x$	19.8 m LiCl	-0.9 to 0.7 V (*vs* Ag/AgCl)	125 F g^{-1} @ 2 mV s^{-1}	Desolvation-free process (Non-SEI)	13
PNTCDA	17M $NaClO_4$	-1.0 to 0.0 V (*vs* Ag/AgCl)	132 @ 20 mA g^{-1}	sluggish ICRR kinetics	14
VO_x@LSG	17.0 M $NaClO_4$ +	-1.4 to 0 V (*vs* Ag/AgCl)	139 @ 0.1 A g^{-1}	sluggish	15

	0.33 M $Na_4Fe(CN)_6$			ICRR kinetics	
Ti_2CT_x	$Li(TFSI)_{0.7}(BETI)_{0.3} \cdot 2H_2O$	-1.1 to 0.0 V (*vs* Ag/AgCl)	60 @ 30 mA g^{-1}	sluggish ICRR kinetics	[16]
V_2CT_x	5 M Ca $(TFSI)_2$	-0.6 to 0.7 V (*vs* Ag/AgCl)	88 @ 0.5 A g^{-1}	Non-SEI (sluggish IAOR)	[7]
Fe_3O_4	21 M LiTFSI	-0.5 to 0.6 V (*vs* RHE)	70 @ 0.1 A g^{-1}	Non-SEI (sluggish IAOR)	[17]
V_2CT_x (current work)	**9 M NaTFSI**	**-0.9 to 0.9 V (*vs* Ag/AgCl)**	**130 @ 0.2 A g^{-1}**	**Non-SEI (sluggish IAOR)**	**This Work**

Abbreviations: $Ti_3C_2T_x$ – Titanium carbide MXene, H_2SO_4 – Sulfuric acid, NaTFSI – Sodium bis(trifluoromethanesulfonyl) imide, V_2CT_x: Vanadium carbide, $NaClO_4$: Sodium perchlorate, Sodium manganese(II) hexacyanoferrate(II), $NaTi_2(PO_3)_4$/ $Ti_3C_2T_x$: Sodium Titanium Phosphate ($NaTi_2(PO_4)_3$) mixed with Titanium Carbide MXene ($Ti_3C_2T_x$), PNTCDA: 3,4,9,10-perylenetetracarboxylic dianhydride, VO_x@LSG: Vanadium oxide@laser scribed graphene, LiTFSI: Lithium bis(trifluoromethanesulfonyl) imide, $Ca(TFSI)_2$: Calcium bis(trifluoromethanesulfonyl) imide, NaMn $[Fe(CN)_6]$: Sodium manganese(II) hexacyanoferrate (II), LiCl:Lithium chloride, $Li(TFSI)_{0.7}(BETI)_{0.3} \cdot 2H_2O$: Lithium bis(trifluoromethanesulfonyl)imide bis(pentafluoroethanesulfonyl)imide dihydrate, $Na_4Fe(CN)_6$: Sodium ferrocycnide, SEI: solid electrolyte interphase. IAOR: Irreversible anodic oxidation reaction, ICRR: Irreversible cathodic reduction reaction.

Table S3. Table showing the size, charge density, Tafel slope and exchange current densities of various charge carriers.

Ionic charge carriers	**Ionic Size (Å)**	**Hydrated size (Å)**	**Charge density**	**Dilute electrolytes**	**Tafel slope (mV dec^{-1})**	**Exchange current density (j_0) (mA cm^{-2})**	**WiSE**	**Tafel slope (mV dec^{-1})**	**Exchange current density (j_0) (mA cm^{-2})**
Li^+	0.76	3.82	+1	1 M LiTFSI	39	0.6	21M LiTFSI	61	0.02
Na^+	1.02	3.58	+1	1 M NaTFSI	47	1.2	9 M NaTFSI	89	0.1
Ca^{2+}	0.99	4.12	+2	1 M $Ca(TFSI)_2$	26	0.4	5 M $Ca(TFSI)_2$	35	$4 * 10^{-4}$
Zn^{2+}	0.74	4.3	+2	1 M $Zn(TFSI)_2$	29	0.3	3M $Zn(TFSI)_2$	40	$2 * 10^{-3}$

Abbreviations: LiTFSI - Lithium bis(trifluoromethanesulfonyl) imide, NaTFSI - Sodium bis(trifluoromethanesulfonyl) imide, $Ca(TFSI)_2$ - Calcium bis(trifluoromethanesulfonyl) imide, $Zn(TFSI)_2$ - Zinc bis(trifluoromethanesulfonyl) imide.

Due to lower the hydration enthalpy, higher will be the exchange current density. The descending order in the hydration enthapy is : $Zn^{2+} > Ca^{2+} > Li^{+} > Na^{+}$. Due to larger ionic radius and lower hydration enthapy, Na^{+} ion showed a larger exchange current density compared to other WiS electrolytes such as Li^{+} and divalent ions (Zn^{2+} and Ca^{2+}).

REFERENCES

1. K. Matthews, T. Zhang, C. E. Shuck, A. VahidMohammadi and Y. Gogotsi, *Chem. Mater.*, 2021, **34**, 499-509.
2. R. Huang, S. Liu, Z. He, W. Zhu, G. Ye, Y. Su, W. Deng and J. Wang, *Adv. Funct. Mater.*, 2022, **32**, 2111661.
3. J. Wang, R. Yu, Y. Jiang, F. Qiao, X. Liao, J. Wang, M. Huang, F. Xiong, L. Cui and Y. Dai, *Energy & Environ. Sci.*, 2024, **17**, 6616-6626.
4. L. Suo, O. Borodin, T. Gao, M. Olguin, J. Ho, X. Fan, C. Luo, C. Wang and K. Xu, *Sci.*, 2015, **350**, 938-943.
5. M. Lounasvuori, T. S. Mathis, Y. Gogotsi and T. Petit, *J. Phy. Chem. Lett.*, 2023, **14**, 1578-1584.
6. X. Hao, L. Zheng, S. Hu, Y. Wu, G. Zhang, B. Li, M. Yang and C. Han, *Mater. Today Energy*, 2023, **38**, 101456.
7. S. Yadav and N. Kurra, *Small*, 2025, **21**, 2503657.
8. Y. Zhang and E. J. Maginn, *J. Phy. Chem. B*, 2021, **125**, 13246-13254.
9. X. Gao, X. Du, T. S. Mathis, M. Zhang, X. Wang, J. Shui, Y. Gogotsi and M. Xu, *Nat. Commun.*, 2020, **11**, 6160.
10. Y. Xia, T. S. Mathis, M.-Q. Zhao, B. Anasori, A. Dang, Z. Zhou, H. Cho, Y. Gogotsi and S. Yang, *Nature*, 2018, **557**, 409-412.
11. K. Nakamoto, R. Sakamoto, M. Ito, A. Kitajou and S. Okada, *Electrochem.*, 2017, **85**, 179-185.
12. C. Yuan, C. Chen, Z. Yang, J. Cheng, J. Weng, S. Tan, R. Hou, T. Cao, Z. Tang, W. Chen, B. Xu, X. Wang and J. Tang, *ACS Appl. Mater. & Interfaces*, 2024, **16**, 55189-55197.
13. X. Wang, T. S. Mathis, Y. Sun, W.-Y. Tsai, N. Shpigel, H. Shao, D. Zhang, K. Hantanasirisakul, F. Malchik, N. Balke, D.-e. Jiang, P. Simon and Y. Gogotsi, *ACS Nano*, 2021, **15**, 15274-15284.
14. Y. Zhang, P. Nie, C. Xu, G. Xu, B. Ding, H. Dou and X. Zhang, *Electrochm. Acta*, 2018, **268**, 512-519.
15. Z. Yang, A. Huang, C.-W. Lin, B. C. Kroes, X. Chang, M. F. El-Kady, Y. Li and R. B. Kaner, *ACS Appl. Mater. & Interfaces*, 2025, **17**, 7595-7606.
16. K. Kim, Y. Ando, A. Sugahara, S. Ko, Y. Yamada, M. Otani, M. Okubo and A. Yamada, *Chem. Mater.*, 2019, **31**, 5190-5196.
17. M. Zhang, Y. Li and Z. Shen, *Journal of Power Sources*, 2019, **414**, 479-485.